Enhanced Magneto-optic Kerr Effect and Magnetic Properties of CeY_{2}Fe_{5}O_{12} Epitaxial Thin Films

Andreas Kehlberger, Kornel Richter, Mehmet C. Onbasli, Gerhard Jakob, Dong Hun Kim, Taichi Goto, Caroline A. Ross, Gerhard Götz, Günter Reiss, Timo Kuschel, and Mathias Kläui

Phys. Rev. Applied **4**, 014008 — Published 20 July 2015

DOI: 10.1103/PhysRevApplied.4.014008

Enhanced magnetooptic Kerr effect and magnetic properties of epitaxial CeYIG thin films

Andreas Kehlberger,[1,*] Kornel Richter,[1] Mehmet C. Onbasli,[2]
Gerhard Jakob,[1] Dong Hun Kim,[2] Taichi Goto,[2] Caroline A. Ross,[2]
Gerhard Götz,[3] Günter Reiss,[3] Timo Kuschel,[3] and Mathias Kläui[1]

[1]*Institute of Physics, University of Mainz, 55099 Mainz, Germany*

[2]*Department of Materials Science and Engineering,*
Massachusetts Institute of Technology,
Cambridge, Massachusetts 02139, USA

[3]*Center for Spinelectronic Materials and Devices,*
Physics Department, Bielefeld University,
Universitätsstrasse 25, 33615 Bielefeld, Germany

(Dated: June 24, 2015)

Abstract

The magnetic and magnetooptic properties of epitaxial $CeY_2Fe_5O_{12}$ (Ce:YIG) and $Y_3Fe_5O_{12}$ (YIG) thin films grown by pulsed laser deposition on gadolinium gallium garnet substrates have been determined. An enhanced Faraday effect is known to result from Ce substitution into the yttrium iron garnet lattice, and here we characterize the magnetooptic Kerr effect as well as the magnetic hysteresis and ferromagnetic resonance response that result from the Ce substitution. X-ray diffraction analysis reveals a high crystallographic quality for the Ce:YIG films. Measurements of the magnetooptic Kerr effect for two different wavelengths demonstrate that the Ce:YIG exhibits an up to tenfold increase in Kerr rotation compared to YIG. The Ce:YIG has a slightly larger magnetic moment as well as an increased magnetic damping and higher magnetic anisotropy compared to YIG with a dependence on the crystalline orientation. By specific cerium substitution in YIG, our results show that the engineering of a large Kerr effect and tailored magnetic anisotropy becomes possible as required for magnetooptically active spintronic devices.

I. INTRODUCTION

Over 50 years ago the discovery of yttrium iron garnet[1,2] ($Y_3Fe_5O_{12}$, YIG) led to remarkable advances in microwave technology. The combination of low magnetic damping, soft magnetization behavior and a bandgap of 2.66 eV, making it a good insulator, qualify this material for microwave applications such as filters[3,4] or sensors.[5,6] Its low absorption in the optical and near-infrared wavelength region combined with a magnetooptic Faraday effect (FE) render this material interesting for telecommunication devices such as magnetooptic isolators[7,8]. For such applications a higher FE is desirable, which allows for the miniaturization of the device.[7,9] With the substitution of yttrium with other rare earth elements like Bismuth or Cerium, it is possible to enhance the FE with only small changes of magnetic moment,[10,11] while the garnet maintains its important property as electrical insulator. The influence of the substitution of Bismuth on the magnetooptic properties has been investigated intensively[12–15], while for Cerium only the FE has been studied in bulk[16–18] and to a lesser extent for thin films.[19–23] However studies on the magnetooptic Kerr effect (MOKE) in Ce:YIG, which is relevant for magnetooptic readout applications that are based on reflection geometry, have not been carried out. As the MOKE in YIG is known to be small for wavelengths in the red and near-infrared spectral range used for optical communications, Ce:YIG thin films are potentially promising, but the MOKE in Ce:YIG needs to be characterized in this wavelength range. An understanding of the magnetic and magnetooptic Kerr behavior of Ce:YIG thin films will facilitate the development of insulating nonreciprocal magnetooptic devices as well as MOKE studies of magnetic phenomena in thin films such as imaging of Eigenmodes in garnets[24,25], which is of particular interest for the development of spin-wave logic.[26]

Previously the effect of cerium substitution on the ferromagnetic resonance (FMR) has been studied, but no reliable reports of the resulting changes in damping have been published due the challenge of growing Ce:YIG without the formation of CeO_2 phases, which disturb the FMR signal.[17] A combination of a strong MOKE signal and low magnetic damping in an insulating material would not only be of interest for magnetooptic applications. This would also allow one to investigate novel phenomena such as domain wall motion in a magnetic insulator, which is in contrast to the well-established domain wall motion in conductors,

not driven by electronic spin currents[27] but by spin-waves.[28,29] Recent results in the field of spin caloritronics have shown that the spin-waves can also be thermally excited by the spin Seebeck effect[30] and are capable of moving magnetic domains.[31–35] However, a more detailed analysis of the thermally excited domain wall motion has not been possible, so far, as experimental observations are currently limited only to bulk materials due to the relatively weak signal in YIG. A stronger MOKE signal of Ce:YIG would enable even studies on thin film nanostructures, which would allow one to gauge the applicability of domain wall motion in memory or logic insulator devices.

Finally for possible applications in spintronics, the magnetic anisotropies in particular need to be controllable. For YIG and other iron garnets, strain has been found to allow the engineering of the anisotropies.[36,37] However element substitution such as Ce doping could provide another approach, which has not been investigated so far but is of interest for all spintronic applications in particular for magnetooptic sensors.[38,39] Tailoring the anisotropy is key as it allows one to determine the orientation of the device.

In this article we present a characterization of epitaxial Ce:YIG ($CeY_2Fe_5O_{12}$) films by superconducting quantum interference device (SQUID) magnetometry, MOKE, MOKE microscopy, FMR as well as crystallographic analysis and compare the results with those of epitaxial YIG ($Y_3Fe_5O_{12}$) thin films with different crystallographic orientations produced by pulsed laser deposition. The results reveal that despite the lattice mismatch, Ce:YIG thin films can be grown with a high quality epitaxially on gadolinium gallium garnet ($Gd_3Ga_5O_{12}$, GGG) substrates. An in-plane magnetic anisotropy can be introduced in this material depending on the substrate cut. Compared to pure YIG, these materials show a slightly higher magnetic moment and as an insulator a damping comparable to magnetic metals. In particular, we find a strongly enhanced MOKE signal for visible wavelengths making the cerium substitution useful for thin film optical devices.

II. EXPERIMENTAL METHODS

The YIG and Ce substituted YIG films were deposited by pulsed laser deposition on single crystalline GGG substrates with (001) and (111) orientations from mixed powder targets of stoichiometry $Y_3Fe_5O_{12}$ and $Ce_1Y_2Fe_5O_{12}$. For target fabrication, the powders were mixed at weights to match the desired stoichiometry and afterwards ground by ball milling (ZrO_2

balls) for 24 hours. Next, the powder was sintered at 1400 °C for 10 hours. After that, the target was calcined at 1150 °C for 12 hours to obtain the YIG or Ce:YIG phase.[19,40]

The optimal deposition conditions for YIG were found for an oxygen deposition pressure of 2.67×10^{-2} mbar (20 mTorr), a substrate temperature of 650 °C and a laser pulse energy of 400 mJ (KrF, $\lambda = 248$ nm) using 10 Hz repetition rate. After the deposition, the YIG films were ex-situ annealed at 800 °C for 5 minutes using rapid thermal annealing under a steady flow of pure oxygen.[40]

For the Ce:YIG films grown at an optimized oxygen pressure of 6.67×10^{-3} mbar (5 mTorr), a substrate temperature of 815 °C and the same pulse energy and repetition rate as for the YIG samples were used. In contrast to the YIG samples, the Ce:YIG samples were not annealed and only cooled down to room temperature at the deposition oxygen pressure. Ce:YIG films were not annealed after PLD growth to preserve the homogeneous distribution of Cerium ions inside the YIG lattice. The crystallographic properties were analyzed using x-ray diffraction (XRD) and x-ray reflectivity (XRR) in a Bruker D8 diffractometer. The saturation moment of each sample was measured by superconducting quantum interference device (SQUID, Quantum Design MPMS XL) at room temperature, while the coercive fields were probed by a vibrating sample magnetometer (VSM). To obtain the magnetic moment M_s of the film, a linear subtraction of the paramagnetic contribution of the GGG substrate background was done.

MOKE magnetometry measurements were carried out in an extended MOKE setup similar to the one described in Ref. 41, but with different wavelengths and a rotatable Wollaston prism combined with two photo-diodes for polarization detection, as used in Ref. 42. For the present study we used linearly polarized light of 406 nm and 635 nm. The angle of incidence was 45 ° for the longitudinal geometry (in-plane external magnetic field) in order to probe the longitudinal MOKE generated by the in-plane magnetization component. Depending on the anisotropies and therefore on the magnetization components during the magnetization reversal process, one can detect an additional polar MOKE component, if the magnetization is not completely in-plane aligned. In order to probe the polar MOKE induced by the out-of-plane magnetization component, additional measurements in the polar geometry (out-of-plane external magnetic field) with perpendicular incident light has been carried out (supplementary information[43]). Magnetooptic imaging of the surface domain structure was performed using an EVICO-ZEISS Imager. A D2m polarizing microscope equipped with

a LED light source provided a continuous spectrum of emitted light in the visible range. Magnetic contrast was obtained by digital image processing in which the background image of the saturation state was subtracted from the sample image in remanence. Magnetic domains were observed after saturation of the sample and subsequent field decrease to zero. The FMR was measured with a Vector Network Analyzer (VNA, Rohde und Schwarz ZVB 40), which was attached to a grounded coplanar waveguide (GCPW). The samples were placed face down on the signal line of the GCPW and the transmission signal S_{21} was recorded. For the measurements, the frequency of the applied signal was swept across the resonance f_{res}, while a fixed in-plane magnetic field was applied. Using the resonance condition for a system with dominating shape anisotropy[44]

$$\Delta f(f) = (|\gamma|\,\mu_0 \Delta H_0 + 2\alpha f)\sqrt{1+\left(\frac{|\gamma|\,\mu_0 M_\mathrm{s}}{2f}\right)^2} \tag{1}$$

we can extract from the measured FMR frequency linewidth the Gilbert damping α and the zero field linewidth broadening. We used the M_s value determined by SQUID magnetometry and a fixed g-factor of $|\gamma| \widehat{=} 28\,\mathrm{GHz/T}$.

III. RESULTS AND DISCUSSION

We characterize the crystalline structure by XRD and our analysis of the YIG and Ce:YIG films did not reveal any secondary phases. The corresponding survey scans are shown in the supplementary information[43]. For Ce:YIG it is significant that no CeO_2 phase was detected, which could arise if the Ce concentration were too high.[17,45] From the positions of the film peaks, shown in Fig. 1, we obtain slightly larger values for the out-of-plane (OOP) lattice constant for YIG compared to the bulk value of 1.2376 nm.[46,47] Compared to unsubstituted YIG the Ce:YIG samples show a 0.2 Å larger out-of-plane lattice constant, implying higher in-plane compressive strain for Ce:YIG on GGG compared to the low strain state of YIG on GGG. The GGG substrates have a lattice constant of 1.2377 nm, which is slightly smaller than the literature value for GGG of 1.2383 nm.[48] The values derived from the $\theta - 2\theta$ scans and the FWHM values of the film are given in Tab. I. Reciprocal space map (RSM) measurements of both Ce:YIG samples are shown in the supplementary information[43]. They reveal a difference for in-plane lattice constants between substrate and film, which hint to a relaxation of the films.

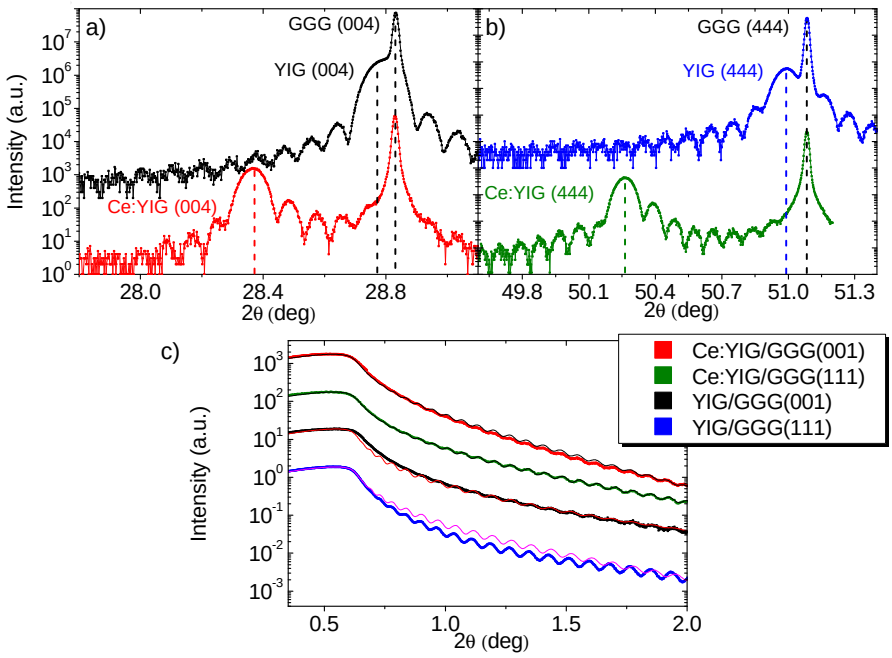

Figure 1. XRD $\theta - 2\theta$ scan of a) YIG and Ce:YIG grown on GGG (001) and b) YIG and Ce:YIG grown on GGG (111). c) XRR measurement as a function of 2θ overlaid with the derived fit functions. The results of the thicknesses derived from the XRR fits are given in Table I. All films show a surface roughness below 1 nm.

For every film we were able to observe Laue oscillations, indicating a good epitaxy of the samples. The Laue oscillations of the Ce:YIG samples show an obvious asymmetry which is a sign of lattice relaxation due to the substrate induced strain. A rocking curve analysis of the Ce:YIG (001) and (111) film peaks corroborates the high quality of the samples, by showing narrow single peaks with a FWHM of only 0.022 ° (GGG substrate peak FWHM $(0.009 \pm 0.002)^\circ$) for both Ce:YIG films, comparable to the FWHM of the YIG films.
The XRR analysis of the films, shown in Fig. 1c), reveals pronounced fringes for all films despite the large film thickness of around 100 nm, indicating very smooth surfaces. The dispersion and absorption values for the Ce:YIG films obtained from the XRR fits are in good agreement with the electron density calculated from the stoichiometry of $Ce_1Y_2Fe_5O_{12}$ and the lattice constants determined from the XRD scans. From these fits we obtain for all films a surface roughness below 1 nm and a higher roughness of around 2 nm for the

Table I. Summary of the results from the XRD and XRR measurements.

Sample	Lattice spacing of OOP reflection (nm) Error 0.001 (nm)	Film peak FWHM (mdeg) Error 0.2 (mdeg)	Thickness (nm) Error 1 (nm)	Surface roughness (nm)
YIG/GGG (001)	1.239	23.9[a]	96	0.5
YIG/GGG (111)	1.240	21.9	97	0.8
Ce:YIG/GGG (001)	1.257	21.3	111	0.7
Ce:YIG/GGG (111)	1.257	22.8	112	0.7

[a] Film peak overlaps with the substrate peak

substrate/film interface. A further surface analysis of the Ce:YIG samples, using atomic force microscopy (AFM), finds fully covered, droplet free surfaces with a RMS roughness of $\sim$ 0.3 nm for both crystallographic orientations. The AFM scans and rocking curve measurements of the Ce:YIG samples are shown in the supplementary information[43], while more information about the YIG film analysis and quality is provided in Ref.[40].

Magnetization curves obtained by SQUID measurements are presented in Fig. 2a) and the derived values such as the saturation magnetic moment and coercive field are given in Table II. While the magnetic moments of the YIG films are close to the literature value of 140 kA/m, the Ce substituted films show an increased magnetic moment of around 155 kA/m. This larger value compared to pure YIG can be explained by the magnetic moment of the Ce^{3+} ions that couple with the magnetic sub-lattices of the Fe^{3+} ions. The Fe^{3+} ions are themselves organized in two sub-lattices (d-site and a-site), which are antiferromagnetically coupled. The net moment is dominated by the d-site for pure YIG. While the Y^{3+} ions possess no magnetic moment, the Ce^{3+} ions are aligned parallel to the d-site Fe^{3+} ions, leading to a higher net magnetic moment.[17,49,50] The higher moment furthermore confirms that no significant CeO_2 phase can be present within our films, as this would lower the moment.[17]

Compared to the pure YIG films, both Ce:YIG samples show a larger coercive field that we detect within the resolution of our SQUID measurements. Since the coercive field is connected to remanent state and the reversal mechanism of the magnetization, we next study the different contributions to the magnetic anisotropy contributions in the Ce:YIG

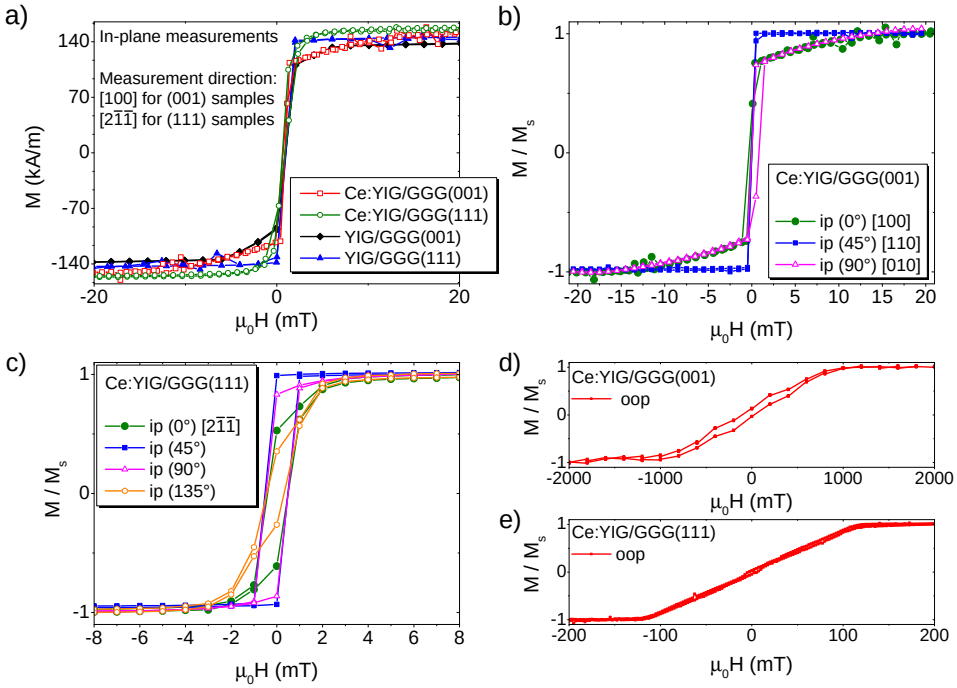

Figure 2. a) SQUID measurements at 300 K of magnetic moment as a function of the applied magnetic in-plane field. The paramagnetic contribution from the GGG substrate has been subtracted. The applied field was along the [100] direction for the samples with (001) orientation and along the the $\left[2\,\bar{1}\,\bar{1}\right]$ for the (111) samples. b) in-plane SQUID loops for Ce:YIG/GGG(001) and c) for Ce:YIG/GGG(111) as a function of the applied magnetic field. The in-plane H-field directions with respect to the in-plane crystallographic axis of the samples are given in the legends. The out-of-plane magnetization curves are shown for Ce:YIG/GGG(001) in d) and for Ce:YIG/GGG(111) in e).

films, which play a key role in applications. The three main contributions to the magnetic free energy density are $f_{\mathrm{sum}} = f_{\mathrm{shape}} + f_{\mathrm{cryst}} + f_{\mathrm{uni}}$ contributing to the effective magnetic anisotropy and we consider these in the following analysis. f_{shape} denotes the demagnetization term by the shape anisotropy, f_{cryst} the contribution of the magnetocrystalline energy, which in case of YIG should yield a cubic anisotropy[51] and f_{uni} marks a uniaxial component, which can be induced by growth, stress or interface effects in thin films. In general pure YIG exhibits only a small magnetic anisotropy, which can be increased by a variation of the stoichiometry[52,53] or a growth-induced magnetoelastic contribution by selection of substrate lattice parameter.[36]

To determine the influence of the Cerium substitution, we perform in-plane angular dependent SQUID, FMR and VSM measurements. A more comprehensive discussion of the magnetic anisotropy and an overview of all angular dependent scans is given in the supplementary information[43], while we will here discuss the key results of these measurements and show as example the angular dependence of the magnetization of the Ce:YIG samples determined by SQUID measurements, presented in Figs. 2b) and c).

The SQUID, VSM and FMR measurements find a four-fold in-plane anisotropy for Ce:YIG films grown on GGG (001) substrates. One of the two easy axes of this cubic anisotropy is oriented along the [110] direction, while the hard axes can be found 45° tilted along [100] and [010]. The symmetry and orientation of anisotropy agrees with projection of the natural cubic anisotropy of the bulk YIG along the $\langle 111 \rangle$ axes[51] to the sample plane. By comparing the saturation field H_s along the [100] direction with the one obtained for YIG/GGG(001), as shown in Fig. 2a), we determine for YIG $H_s = 7\,\mathrm{mT}$ and for Ce:YIG $H_s = 17\,\mathrm{mT}$. The further angular dependent measurements, shown in the supplementary information[43], reveal an additional uniaxial in-plane magnetic anisotropy of $H_u \leq 1\,\mathrm{mT}$, causing a contribution too weak to be resolved within the resolution of the SQUID measurements. From the SQUID measurements one only obtains the effective magnetization energy, given in Table II, which results of the sum of all contributing terms. Due to the small in-plane contribution of the uniaxial anisotropy we can neglect this term, which allows us to use the SQUID saturation field values H_s to extract directly the cubic anisotropy constant from H_s measured along the hard axes [100] and [010] by using $K_{cub} = -H_s \mu_0 M_s/2$[51]. Using this formula we derive an increase of the cubic in-plane anisotropy by a factor of three compared to our pure YIG films, giving $K_{cub,Ce:YIG} = (-1.3 \pm 0.1)\mathrm{kJ/m^3}$ and $K_{cub,YIG} = (-0.5 \pm 0.1)\mathrm{kJ/m^3}$.

The SQUID measurements of one of our Ce:YIG/GGG(111) samples reveal a magnetic hard axis along the 135 ° direction and an easier axis along 45 ° compared to the 0 ° direction (which corresponds to the in-plane crystalline $[2\,\overline{1}\,\overline{1}]$ orientation), as shown in Fig. 2c). This symmetry indicates an in-plane uniaxial anisotropy contribution. The angular dependent FMR measurements confirm this assumption as they yield an in-plane two-fold symmetry as well for the anisotropy, hinting to a dominating in-plane uniaxial anisotropy. From the crystalline surface symmetry one would expect a six-fold anisotropy, which is observed in VSM measurements of thinner samples[54]. The origin of the uniaxial anisotropy can be explained by influence of the substrate surface as is evident from further XRD measurements,

shown in the supplementary information[43]. The XRD measurements find a maximum for the miscut between the substrate normal and film orientation of only 0.1 °, which matches with the orientation of the magnetic hard axis. These results highlight the importance of the substrate surface topography, as already a small miscut of only 0.1° can cause a dominating anisotropy term. This result is similar to earlier investigations for standard YIG films[55], for which a larger miscut has been found to be the origin of an observed uniaxial magnetic anisotropy.

For the determination of the out-of-plane magnetization, we perform SQUID and polar MOKE magnetometry measurements, shown in Fig. 2d), e) and in more detail in the supplementary information[43]. For both crystalline orientations we observe a hard axis-like behavior of the magnetization. The out-of-plane SQUID measurement of Ce:YIG/GGG(001) sample yields a saturation field of $H_\mathrm{s} = (1 \pm 0.1)\mathrm{T}$, in good agreement with the FMR results. The origin of this anisotropy might be a combination of surface, shape and magnetoelastic anisotropy. The observed saturation field for Ce:YIG/GGG(111) of $H_\mathrm{s} = (120 \pm 10)\,\mathrm{mT}$ is lower than the combination of shape and uniaxial in-plane anisotropy, indicating a further contribution of an anisotropy favoring an out-of-plane magnetization. The origin of this complex anisotropy behavior possibly results from the epitaxial growth on the GGG substrate having a smaller in-plane lattice constant, leading to magnetoelastic contribution to the anisotropy. RSM measurements indicate that the Ce:YIG films undergo relaxation as the film thickness increases, making an estimation of the magnetoelastic contribution difficult due to an inhomogeneous strain within the layer thickness. Further studies of thinner, non relaxed Ce:YIG films should aim to determine the influence of the Ce substitution in combination with epitaxial growth on substrates with a smaller in-plane lattice constant, such as Yttrium Aluminum Garnet (YAG)[36]. In combination with a variation of the Ce amount, this might allow one to increase the out-of-plane magnetic anisotropy and still maintain epitaxial growth but this is beyond the scope of the current work presented here. Using these methods it should be possible to adapt the anisotropy to satisfy the requirements of the desired application such as a magnetooptic sensor.[39]

Next we describe the magnetooptic properties of the Ce:YIG. Fig. 3a) shows drastically increased MOKE signals for Ce:YIG compared to pure YIG for a wavelength of $\lambda = 635\,\mathrm{nm}$. While the magnitude of the Kerr rotation of YIG at this wavelength was below 2 mdeg

Table II. Summary of the results from SQUID magnetometry. H_c denotes the coercive field, $H_{s,ip}$ the in-plane and $H_{s,oop}$ out-of-plane saturation field determined for the hard axis. The angle marked behind the value denotes the in-plane orientation of the hard axis. The anisotropy constants were calculated from the anisotropy fields extracted from the SQUID measurements using $K_{eff} = \mu_0 M_s H_s/2$.

Sample	M_s (kA/m)	H_c (mT)	$H_{s,ip}$ (mT)	$K_{eff,ip}$ (kJ/m^3)	$H_{s,oop}$ (T)	$K_{eff,oop}$ (kJ/m^3)
YIG/GGG (001)	139 ± 7	<0.5	$6.5 \pm 1\,(0°)$	0.5 ± 0.1	-	-
YIG/GGG (111)	144 ± 7	<0.5	-	-	-	-
Ce:YIG/GGG (001)	152 ± 8	0.3 ± 0.2	$17.1 \pm 1\,(0°, 90°)$	1.3 ± 0.1	1 ± 0.1	76 ± 9
Ce:YIG/GGG (111)	158 ± 8	0.5 ± 0.1	$5 \pm 1\,(135°)$	0.4 ± 0.1	0.12 ± 0.01	9.5 ± 0.9

for both orientations, it increased to 26 mdeg for Ce:YIG/GGG(001) and to 38 mdeg for Ce:YIG/GGG(111). As seen in Fig. 3b), at $\lambda = 406$ nm, we observe a larger Kerr magnitude of 16 mdeg for both YIG samples. Ce:YIG shows an even larger effect with a Kerr rotation of 37 mdeg for (001) and 46 mdeg for (111), i.e. the Ce:YIG exhibited a 200% higher signal compared to YIG. Bulk YIG has a bandgap of 2.66 eV $\hat{=}$ 466 nm and a similar bandgap is present for Ce:YIG.[20]

These MOKE results show that the enhancement of the magnetooptic constants known from the Faraday effect for Ce:YIG[19–22], is also present for the Kerr effect, which makes Ce:YIG a useful material for nonreciprocal devices. Furthermore the substitution by Cerium expands the range of useable wavelengths far into the optical wavelength region, allowing us to use optically operated devices in reflection geometry for the read out of the magnetic structure, including high resolution MOKE microscopy.

Using the enhanced MOKE results, we now compare the magnetic anisotropy information from MOKE hysteresis and domain images with the results obtained by the SQUID measurements. For both wavelengths, a noticeable difference in the hysteresis loops between the two crystalline orientations of Ce:YIG can be observed. Ce:YIG/GGG(111) shows higher MOKE signals than Ce:YIG/GGG(001) for both wavelengths, and larger coercive fields for (111) vs. (001) which is the opposite trend compared to the SQUID results.

The MOKE measurements for YIG and Ce:YIG on GGG(001) were done with an external

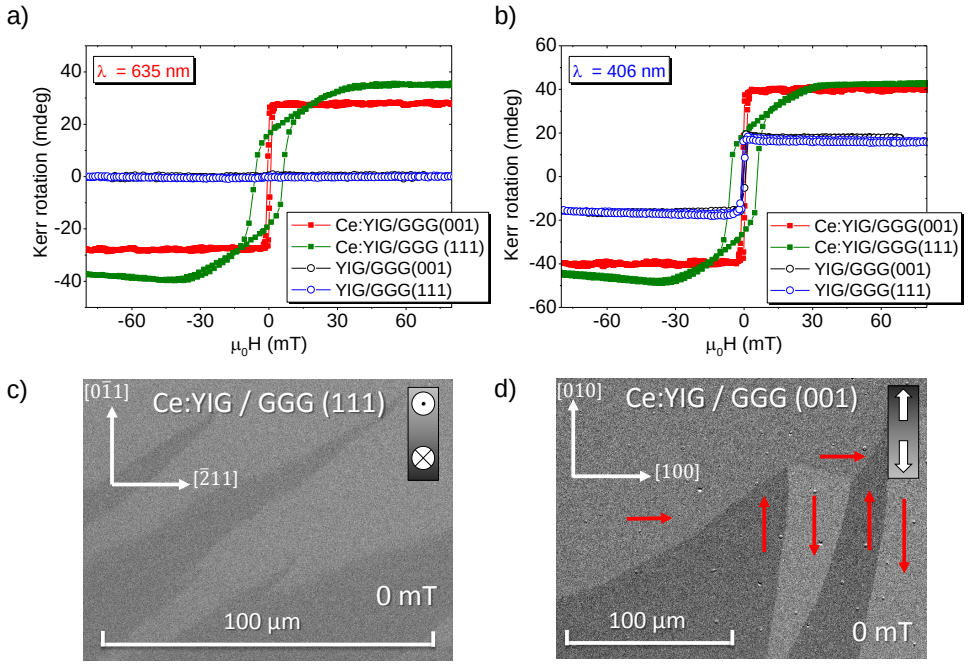

Figure 3. (a,b) MOKE signal of YIG and Ce:YIG as a function of the applied magnetic field for a laser wavelength of a) $\lambda = 635\,\mathrm{nm}$ and b) $\lambda = 406\,\mathrm{nm}$. The MOKE signals were recorded for Ce:YIG/GGG(001) with the external magnetic fields along the [110] direction and for Ce:YIG/GGG(111) along the $[2\,\bar{1}\,\bar{1}]$ direction. From the MOKE loops we extract $H_c = (0.7 \pm 0.1)\,\mathrm{mT}$ for Ce:YIG/GGG(001), $H_c = (5.8 \pm 0.3)\,\mathrm{mT}$ for Ce:YIG/GGG(111), $H_c = (0.5 \pm 0.1)\,\mathrm{mT}$ for YIG/GGG(001) and $H_c = (0.5 \pm 0.1)\,\mathrm{mT}$ for YIG/GGG(111). (c,d) MOKE microscopy image of the boundary between the magnetic domain structures that result from the different anisotropies in c) the Ce:YIG/GGG(111) sample observed in polar MOKE configuration and d) Ce:YIG/GGG(001) sample observed by longitudinal MOKE. The red arrows correspond to the alignment of the in-plane magnetization.

magnetic field along the [110] direction, and the hysteresis loop has the same high squareness as in the [110] SQUID measurements, shown in Fig. 2c). The longitudinal MOKE microscopy images presented in Fig. 3d) show a domain pattern that can be explained by a four-fold in-plane anisotropy in combination with a two-fold anisotropy[56], which is consistent with the lattice symmetry and the SQUID and FMR data, shown in the supplementary information[43]. Finally it is important to mention a symmetric contribution with respect to the external magnetic field for the magnetization curves of the YIG samples at $\lambda = 406\,\mathrm{nm}$

in Fig. 3b). As reported for example for Co-based Heusler compounds[57], this effect is generated by quadratic MOKE contributions and deforms the magnetization curves.
The MOKE hysteresis for the Ce:YIG/GGG(111) sample was measured along $[2\,\overline{1}\,\overline{1}]$. The different loop shape compared to the SQUID data is most likely a result of contributions of the out-of-plane magnetization component (and therefore of the polar MOKE) to the longitudinal MOKE signals[58], as the measurements were taken under 45 ° angle of incidence. A polar MOKE microscopy image, shown in Fig. 3c), revealed a domain structure indicating a nonzero remanence in the out-of-plane direction. The observed domain shape is consistent with the presence of an in-plane uniaxial anisotropy.
The enhanced magnetooptic contrast allows us to verify our SQUID results for the magnetic anisotropy. Further it shows that the Ce substitution allows one to investigate the magnetic domain structure even in thin films, which is of particular interest as garnets are known for more complex domain structures like for the formation of magnetic bubble skyrmion[59].
Having established the magnetostatic properties, one needs to study the spin dynamics and in particular the damping parameter of the material, in order to be able to use the material in spintronic devices.

In order to provide the answer to this missing piece of information, we finally study the magnetodynamic properties to gauge the high frequency performance of Ce:YIG. FMR response as a function of the frequency is presented for Ce:YIG in Fig. 4a) and for YIG in Fig. 4b). Despite the fact that all films have a similar thickness of approximately 100 nm, the Ce:YIG shows in general a more than one order of magnitude lower FMR peak and two orders of magnitude wider resonance linewidths. This leads to the experimental challenge that the FMR signals of the Ce:YIG are comparable to those of the paramagnetic background signal caused by the GGG substrates, which makes it necessary to consider a linear contribution for the resonance peak for high magnetic fields.
Fitting a Lorentz peak function to the absolute signal, we obtain the FMR linewidth plotted in Fig. 4c). As the slope of Δf is only slightly affected by any magnetic anisotropy, Eq. 1 allows us to extract a good estimate of the Gilbert damping of the material as shown in Table III. For our 100 nm thick YIG films we observe a difference between the two crystalline orientations. While the Gilbert damping constant α was $2.6 \cdot 10^{-4}$ for the (001) orientation, the damping as well as ΔH_0 are increased by a factor of 2 for the (111) orientation. The exact values are given in Table III. We expect that the enhanced damping is the result of a

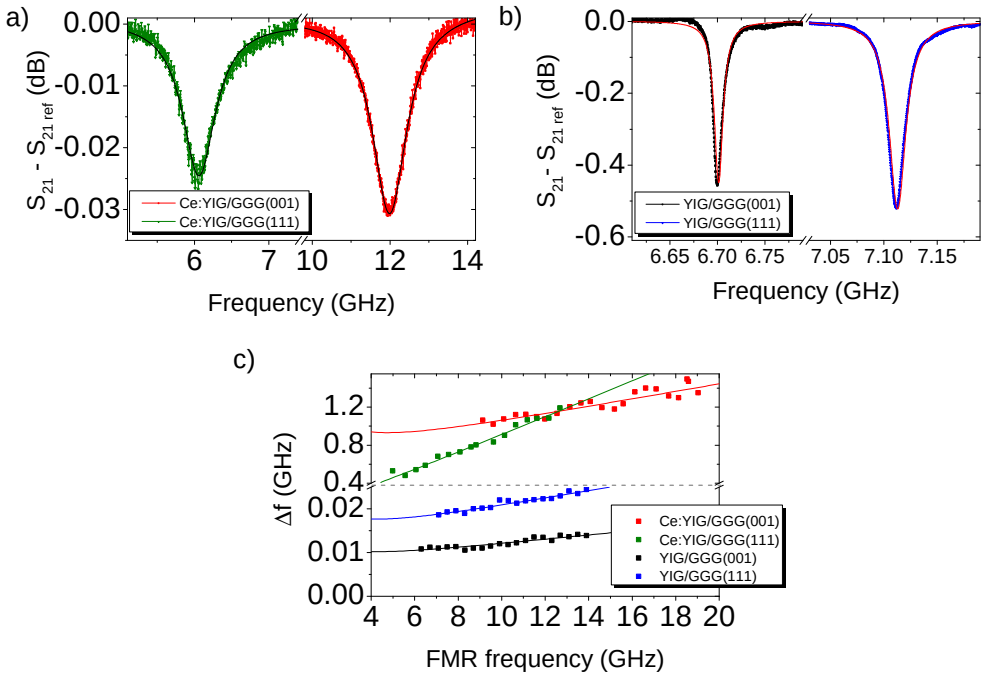

Figure 4. a) FMR signal as function of frequency for a) Ce:YIG at an external magnetic field of $\mu_0 H = 160\,\mathrm{mT}$ and for b) YIG at an external magnetic field of $\mu_0 H = 170\,\mathrm{mT}$. The fitted Lorentz peak function is superposed. From the fit we obtain a FWHM of 1.07 GHz for Ce:YIG(001), 0.54 GHz for Ce:YIG(111), 11.1 MHz for YIG(001) and 18.7 MHz for YIG(001). c) FMR frequency linewidth Δf_{res} as function of FMR frequency f_{res} combined with the derived fit functions of Eq.1. The data were obtained for external magnetic field along the [100] direction for the samples with the (001) orientation and along $\left[2\,\bar{1}\,\bar{1}\right]$ for the (111) samples.

more complex growth condition for the (111) interface and lower crystalline perfection, which would need further optimization, while the value for the (001) oriented film is remarkably low.[40]

Both Ce:YIG samples show two orders of magnitude higher Gilbert damping of the order of 10^{-2} as well as increased zero field broadening compared to YIG. The observed increase by two orders of magnitude for α can be explained as sum of different contributions. Firstly, the Ce^{3+} substitution leads to an expanded crystal lattice, which also affects the Fe sublattice, and leads to tetragonal distortion in the epitaxial films on GGG. Second the magnetic moment carried by the Ce^{3+} leads to a perturbation of the Fe sublattices. Thirdly the Ce^{3+} substitution, which only occupies one third of the lattice sites and is not expected to be

h

Table III. Summary of the results from FMR measurements. The resonance fits based on Eq. 1 used the M_s obtained from the SQUID measurements, given in Table II.

Sample	$\mu_0 \Delta H_0$ (mT)	$\alpha\,(10^{-4})$
YIG/GGG (001)	0.24 ± 0.04	2.6 ± 0.4
YIG/GGG (111)	0.41 ± 0.06	4.4 ± 0.7
Ce:YIG/GGG (001)	22 ± 4	200 ± 40
Ce:YIG/GGG (111)	-2.9 ± 3	480 ± 70

ordered, will lead to different environments for the Fe ions. Finally, we also find a noticeable increase of α for Ce:YIG(111) compared to the (001) orientation, similar to the observation for YIG. Again this result hints towards a more complex growth condition on the GGG(111) substrates. Despite the higher damping in the insulating Ce:YIG films, we can still observe a clear FMR signal[15] and a damping that is similar to magnetic metals[60,61]. This damping constant is low enough to allow for fast switching in competitive devices. Furthermore as Ce:YIG maintains the good insulating properties of YIG, no ohmic losses for instance due to eddy currents occur and magnonic spin currents can propagate with ultralow power dissipation.

IV. CONCLUSION

The crystalline, magnetooptic and magnetic properties of Ce:YIG films on GGG are determined for (001) and (111) crystallographic orientations and compared with those of YIG films. The XRD curves of the Ce:YIG samples show Laue oscillations, a surface roughness below 1 nm and very narrow rocking curves of 0.022 ° indicating a high crystalline quality, but also a lattice strain induced by the mismatch with the GGG substrates. Our SQUID measurements show that Ce substitution only slightly increases the total magnetic moment by 10 kA/m. All magnetic characterization methods reveal that the substitution by Ce causes a higher magnetic anisotropy compared to pure YIG, which in the case of Ce:YIG/GGG(001) has a four-fold in-plane component and a more complex anisotropy for the Ce:YIG/GGG(111), showing that anisotropies can be tailored in this material. The spin

dynamics are studied by VNA-FMR and measurements of the thin films revealed that our high quality films exhibit a magnetic damping comparable to magnetic metals of $\alpha = 4{\cdot}10^{-2}$. In contrast to usual magnetooptic investigation of garnets which focuses on the Faraday effect, we study the magnetooptic Kerr effect which enables thin film magnetooptic devices, which is desirable for some designs of integrated magnetooptic devices such as isolators[9,62,63] or circulators[7]. In particular MOKE measurements of Ce:YIG reveal an increase of a factor two of the Kerr rotation for $\lambda = 406\,\mathrm{nm}$, compared to pure YIG, and a tenfold increase of the Kerr rotation for $\lambda = 635\,\mathrm{nm}$. This first investigation of the MOKE in this material shows that the MOKE is significant for both wavelengths demonstrating the broader applicability of this material for magnetooptic devices, like sensors[38,39] and allows for high resolution magnetooptic imaging. Our magnetic microscopy reveals a strong contrast for the different magnetic domain orientations, highlighting that in addition to applications this insulating material provides an excellent research basis for investigation of complex magnetic phenomena like the magnetooptic imaging of magnetostatic spin-wave Eigenmodes[24,25] and the domain wall motion due to magnonic spin-currents[28,33]. Our results show that by using the Ce substitution of YIG for tailoring the magnetic properties and magnetooptic properties one obtains a further novel toolkit for engineering the magnetic properties depending on the demand of applications.

ACKNOWLEDGMENTS

The authors would like to thank the Deutsche Forschungsgemeinschaft (DFG) for financial support via SPP 1538 "Spin Caloric Transport", the Graduate School of Excellence Materials Science in Mainz (MAINZ) GSC 266, the German Ministry for Education and Science "Mainz-MIT Seed Fund" (BMBF 01DM12012), the EU (IFOX, NMP3-LA-2012246102, INSPIN, FP7-ICT-2013-X 612759, MASPIC, ERC-2007-StG 208162), the National Science Foundation and FAME, a STARnet Center of DARPA and MARCO.

---

* Graduate School Materials Science in Mainz, Staudinger Weg 9, 55128, Germany

[1] F. Bertaut and F. Forrat, "Structure of ferrimagnetic rare-earth ferrites," C.R. Acad. Sci., Paris **242**, 382 (1956).

[2] S. Geller and M. A. Gilleo, "Structure and ferrimagnetism of yttrium and rare-earth–iron garnets," Acta Crystallogr. **10**, 239 (1957).

[3] P. Röschmann, "Compact YIG Bandpass Filter with Finite-Pole Frequencies for Applications in Microwave Integrated Circuits," IEEE Trans. Microwave Theory Tech. **21**, 52–57 (1973).

[4] Y. Murakami, T. Ohgihara, and T. Okamoto, "A 0.5-4.0-GHz Tunable Bandpass Filter Using YIG Film Grown by LPE," IEEE Trans. Microwave Theory Tech. **35**, 1192–1198 (1987).

[5] M.N. Deeter, A.H. Rose, and G.W. Day, "Fast, sensitive magnetic-field sensors based on the Faraday effect in YIG," J. Lightw.Technol. **8**, 1838–1842 (1990).

[6] S. Higuchi, K. Ueda, F. Yahiro, Yoshiki Nakata, H. Uetsuhara, T. Okada, and Mitsuo Maeda, "Fabrications of cerium-substituted YIG thin films for magnetic field sensor by pulsed-laser deposition," IEEE Trans. Magn **37**, 2451–2453 (2001).

[7] Y. Shoji, T. Mizumoto, H. Yokoi, I-W. Hsieh, and R. M. Osgood, "Magneto-optical isolator with silicon waveguides fabricated by direct bonding," Appl. Phys. Lett. **92**, 071117 (2008).

[8] B.J.H. Stadler and T. Mizumoto, "Integrated Magneto-Optical Materials and Isolators: A Review," IEEE Photon. J. **6**, 1–15 (2014).

[9] M.-C. Tien, T. Mizumoto, P. Pintus, H. Kromer, and J. E. Bowers, "Silicon ring isolators with bonded nonreciprocal magneto-optic garnets," Opt. Express **19**, 11740–11745 (2011).

[10] N.B. Ibrahim, C. Edwards, and S.B. Palmer, "Pulsed laser ablation deposition of yttrium iron garnet and cerium-substituted YIG films," J. Magn. Magn. Mater. **220**, 183 – 194 (2000).

[11] P. Hansen and J.-P. Krumme, "Magnetic and magneto-optical properties of garnet films," Thin Solid Films **114**, 69 – 107 (1984), special Issue on Magnetic Garnet Films.

[12] P. Hansen, K. Witter, and W. Tolksdorf, "Magnetic and magneto-optic properties of lead- and bismuth-substituted yttrium iron garnet films," Phys. Rev. B **27**, 6608–6625 (1983).

[13] M. Deb, E. Popova, A. Fouchet, and N. Keller, "Magneto-optical faraday spectroscopy of completely bismuth-substituted bi 3 fe 5 o 12 garnet thin films," J. Phys. D: Appl. Phys. **45**, 455001 (2012).

[14] S. Defang, D. Tengda, Z. Yong, Z. Minjuan, C. Bin, and Z. Weizhu, "Magnetic and magneto-optical properties of bi-substituted garnet films," J. Magn. Magn. Mater. **135**, 241 – 250 (1994).

[15] A. Sposito, S. A. Gregory, P. A. J. de Groot, and R. W. Eason, "Combinatorial pulsed laser deposition of doped yttrium iron garnet films on yttrium aluminium garnet," J. Appl. Phys. **115**, 053102 (2014).

[16] M. Huang and S.-Y. Zhang, "Growth and characterization of cerium-substituted yttrium iron garnet single crystals for magneto-optical applications," Appl. Phys. A **74**, 177–180 (2002).

[17] T.-C. Mao and J.-C. Chen, "Influence of the addition of CeO2 on the microstructure and the magnetic properties of yttrium iron garnet ceramic," J. Magn. Magn. Mater. **302**, 74 – 81 (2006).

[18] T.-C. Mao, J.-C. Chen, and C.-C Hu, "Effect of the pulling rate on the quality of cerium-substituted YIG single-crystal fibers by LHPG," J. Crystal Growth **296**, 110 – 116 (2006).

[19] T. Goto, M. C. Onbaşli, and C. A. Ross, "Magneto-optical properties of cerium substituted yttrium iron garnet films with reduced thermal budget for monolithic photonic integrated circuits," Opt. Express **20**, 28507–28517 (2012).

[20] T. Goto, Y. Eto, K. Kobayashi, Y. Haga, M. Inoue, and C. A. Ross, "Vacuum annealed cerium-substituted yttrium iron garnet films on non-garnet substrates for integrated optical circuits," J. Appl. Phys. **113**, 17A939 (2013).

[21] M. Gomi, H. Furuyama, and M. Abe, "Strong magnetooptical enhancement in highly Ce substituted iron garnet films prepared by sputtering," J. Appl. Phys. **70**, 7065 (1991).

[22] M. Gomi, H. Toyoshima, and T. Yamada, "Magneto-Optical Properties of Pr, Ni- and Ce, Ni-Substituted YIG Epitaxial Films Prepared by Sputtering," J. Phys. IV France **7**, C1–723 – C1–724 (1997).

[23] L. Bi, J. Hu, P. Jiang, D. H. Kim, G. F. Dionne, L. C. Kimerling, and C. A. Ross, "On-chip optical isolation in monolithically integrated non-reciprocal optical resonators," Nature Photon. **5**, 75862 (2011).

[24] M. Buess, R. Höllinger, T. Haug, K. Perzlmaier, U. Krey, D. Pescia, M. R. Scheinfein, D. Weiss, and C. H. Back, "Fourier Transform Imaging of Spin Vortex Eigenmodes," Phys. Rev. Lett. **93**, 077207 (2004).

[25] I. Neudecker, M. Kläui, K. Perzlmaier, D. Backes, L. J. Heyderman, C. A. F. Vaz, J. A. C. Bland, U. Rüdiger, and C. H. Back, "Spatially Resolved Dynamic Eigenmode Spectrum of Co Rings," Phys. Rev. Lett. **96**, 057207 (2006).

[26] M. P. Kostylev, A. A. Serga, T. Schneider, B. Leven, and B. Hillebrands, "Spin-wave logical gates," Appl. Phys. Lett. **87**, 153501 (2005).

[27] M. Hayashi, L. Thomas, R. Moriya, C. Rettner, and S. S. P. Parkin, "Current-Controlled Magnetic Domain-Wall Nanowire Shift Register," Science **320**, 209–211 (2008).

[28] D.-S. Han, S.-K. Kim, J.-Y. Lee, S. J. Hermsdoerfer, H. Schultheiss, B. Leven, and B. Hillebrands, "Magnetic domain-wall motion by propagating spin waves," Appl. Phys. Lett. **94**, 112502 (2009).

[29] J.-S. Kim, M. Stärk, M. Kläui, J. Yoon, C.-Y. You, L. Lopez-Diaz, and E. Martinez, "Interaction between propagating spin waves and domain walls on a ferromagnetic nanowire," Phys. Rev. B **85**, 174428 (2012).

[30] K. Uchida, H. Adachi, T. Ota, H. Nakayama, S. Maekawa, and E. Saitoh, "Observation of longitudinal spin-Seebeck effect in magnetic insulators," Appl. Phy. Lett. **97**, 172505 (2010).

[31] P. Möhrke, J. Rhensius, J.-U. Thiele, L.J. Heyderman, and M. Kläui, "Tailoring laser-induced domain wall pinning," Solid State Commun. **150**, 489 – 491 (2010).

[32] X. S. Wang and X. R. Wang, "Thermodynamic theory for thermal-gradient-driven domain-wall motion," Phys. Rev. B **90**, 014414 (2014).

[33] D. Hinzke and U. Nowak, "Domain Wall Motion by the Magnonic Spin Seebeck Effect," Phys. Rev. Lett. **107**, 027205 (2011).

[34] U. Ritzmann, D. Hinzke, and U. Nowak, "Propagation of thermally induced magnonic spin currents," Phys. Rev. B **89**, 024409 (2014).

[35] W. Jiang, P. Upadhyaya, Y. Fan, J. Zhao, M. Wang, L.-T. Chang, M. Lang, K. L. Wong, M. Lewis, Y.-T. Lin, J. Tang, S. Cherepov, X. Zhou, Y. Tserkovnyak, R. N. Schwartz, and K. L. Wang, "Direct Imaging of Thermally Driven Domain Wall Motion in Magnetic Insulators," Phys. Rev. Lett. **110**, 177202 (2013).

[36] P. C. Hammel H. Wang, C. Du and F. Yang, "Strain-tunable magnetocrystalline anisotropy in epitaxial Y3Fe5O12 thin films," Phys. Rev. B. **89**, 134404 (2014).

[37] M. Kubota, A. Tsukazaki, F. Kagawa, K. Shibuya, Y. Tokunaga, M. Kawasaki, and Y. Tokura, "Stress-Induced Perpendicular Magnetization in Epitaxial Iron Garnet Thin Films," Appl. Phys. Express **5**, 103002 (2012).

[38] S. Higuchi, Y. Furukawa, S. Takekawa, O. Kamada, K. Kitamur, and K. Uyeda, "Magnetooptical properties of cerium-substituted yttrium iron garnet single crystals for magnetic-field sensor," Sensors and Actuators A **105**, 293 – 296 (2003).

[39] O. Kamada, T. Nakaya, and S. Higuchi, "Magnetic field optical sensors using Ce:YIG single crystals as a Faraday element," Sensors and Actuators A **119**, 345 – 348 (2005).

[40] M. C. Onbasli, A. Kehlberger, D. H. Kim, G. Jakob, M. Kläui, A. V. Chumak, B. Hillebrands, and C. A. Ross, "Pulsed laser deposition of epitaxial yttrium iron garnet films with low Gilbert damping and bulk-like magnetization," Appl. Phys. Lett. Mat. **2**, 106102 (2014).

[41] T. Kuschel, H. Bardenhagen, H. Wilkens, R. Schubert, J. Hamrle, J. Pištora, and J. Wollschläger, "Vectorial magnetometry using magnetooptic Kerr effect including first- and second-order contributions for thin ferromagnetic films," J. Phys. D: Appl. Phys. **44**, 265003 (2011).

[42] S. Trudel, G. Wolf, H. Schultheiss, J. Hamrle, and B. Hillebrands, "Probing quadratic magneto-optical Kerr effects with a tandem dual-beam system," Rev. Sci. Instrum. **81**, 026105 (2010).

[43] See Supplemental Material at [URL] for further information about crystallographic, surface and magnetic anisotropy analysis.

[44] S. S. Kalarickal, P. Krivosik, M. Wu, C. E. Patton, M. L. Schneider, P. Kabos, T. J. Silva, and J. P. Nibarger, "Ferromagnetic resonance linewidth in metallic thin films: Comparison of measurement methods," J. Appl. Phys. **99**, 093909 (2006).

[45] S. M. Shahrokhvand, A. S. H. Rozatian, M. Mozaffari, S. M. Hamidi, and M. M. Tehranchi, "Preparation and investigation of Ce:YIG thin films with a high magneto-optical figure of merit," J. Phys. D: Appl. Phys. **45**, 235001 (2012).

[46] R. C. Linares, R. B. McGraw, and J. B. Schroeder, "Growth and Properties of Yttrium Iron Garnet Single-Crystal Films," J. Appl. Phys. **36**, 2884 (1965).

[47] F. Euler and J. A. Bruce, "Oxygen coordinates of compounds with garnet structure," Acta Crystallogr. **19**, 971 (1965).

[48] H. Sawada, "Electron Density Study of Garnets: Z3Ga5O12;Z = Nd, Sm, Gd, Tb," J. Solid State Chem. **132**, 300 (1997).

[49] T. Sekijima, H. Kishimoto, T. Fujii, K. Wakino, and M. Okada, "Magnetic, Optical and Microwave Properties of Rare-Earth-Substituted Fibrous Yttrium Iron Garnet Single Crystals Grown by Floating Zone Method," Jpn. J. Appl. Phys. **38**, 5874 (1999).

[50] H. Xu and H. Yang, "Magnetic properties of YIG doped with cerium and gadolinium ions," J. Mater. Sci.: Mater. Electron **19**, 589–593 (2008).

[51] G. F. Dionne, *Magnetic Oxides*, Springer Science+Business Media , pp.232 (2009).

[52] S. A. Manuilov, S. I. Khartsev, and A. M. Grishin, "Pulsed laser deposited Y3Fe5O12 films: Nature of magnetic anisotropy I," J. Appl. Phys. **106**, 123917 (2009).

[53] S. A. Manuilov and A. M. Grishin, "Pulsed laser deposited Y3Fe5O12 films: Nature of magnetic anisotropy II," J. Appl. Phys. **108**, 013902 (2010).

[54] M.C. Onbasli, L. Beran, M. Zahradnik, M. Kučera, R. Antoš, J. Mistrik, G. F. Dionne, M. Veis, and C. A. Ross, "Optical and magneto-optical behavior of cerium yttrium iron garnet thin films at wavelengths of 200 - 1770 nm," submitted (2015).

[55] A. Kehlberger, G. Jakob, M. C. Onbasli, D. H. Kim, C. A. Ross, and M. Kläui, "Investigation of the magnetic properties of insulating thin films using the longitudinal spin Seebeck effect," J. Appl. Phys. **115**, 17C731 (2014).

[56] S. Mallik, N. Chowdhury, and S. Bedanta, "Interplay of uniaxial and cubic anisotropy in epitaxial Fe thin films on MgO (001) substrate," AIP Advances **4**, 097118 (2014).

[57] J. Hamrle, S. Blomeier, O. Gaier, B. Hillebrands, H. Schneider, G. Jakob, K. Postava, and C. Felser, "Huge quadratic magneto-optical Kerr effect and magnetization reversal in the Co2FeSi Heusler compound," J. Phys. D: Appl. Phys. **40**, 1563 (2007).

[58] H.F. Ding, S. Pütter, H.P. Oepen, and J. Kirschner, "Experimental method for separating longitudinal and polar Kerr signals," J. Magn. Magn. Mater. **212**, L5–L11 (2000).

[59] A. P. Malozemoff, J. C. Slonczewski, and R. Wolfe, *Magnetic Domain Walls in Bubble Materials*, John Wiley and Sons , pp.8 (1979).

[60] J. Walowski, M. D. Kaufmann, B. Lenk, C. Hamann, J. McCord, and M. Münzenberg, "Intrinsic and non-local Gilbert damping in polycrystalline nickel studied by Ti:sapphire laser fs spectroscopy," J. Phys. D: Appl. Phys. **41**, 164016 (2008).

[61] M. Farle, "Ferromagnetic resonance of ultrathin metallic layers," Rep. Prog. Phys. **61**, 755 (1998).

[62] T. Shintaku, T. Uno, and M. Kobayashi, "Magneto-optic channel waveguides in Ce-substituted yttrium iron garnet," J. Appl. Phys. **74**, 4877–4881 (1993).

[63] H. Dötsch, N. Bahlmann, O. Zhuromskyy, M. Hammer, L. Wilkens, R. Gerhardt, P. Hertel, and A. F. Popkov, "Applications of magneto-optical waveguides in integrated optics: review," J. Opt. Soc. Am. B **22**, 240–253 (2005).